PHYSICAL REVIEW B **100**, 224306 (2019)

Hofstadter butterfly in a cavity-induced dynamic synthetic magnetic field

Elvia Colella,[1,*] Farokh Mivehvar,[1] Francesco Piazza,[2] and Helmut Ritsch[1]
[1]*Institut für Theoretische Physik, Universität Innsbruck, A-6020 Innsbruck, Austria*
[2]*Max-Planck-Institut für Physik komplexer Systeme, D-01187 Dresden, Germany*

(Received 22 October 2019; revised manuscript received 10 December 2019; published 23 December 2019)

Energy bands of electrons in a square lattice potential threaded by a uniform magnetic field exhibit a fractal structure known as the Hofstadter butterfly. Here we study a Fermi gas in a 2D optical lattice within a linear cavity with a tilt along the cavity axis. The hopping along the cavity axis is only induced by resonant Raman scattering of transverse pump light into a standing-wave-cavity mode. Choosing a suitable pump geometry allows us to realize the Hofstadter-Harper model with a cavity-induced dynamical synthetic magnetic field, which appears at the onset of the superradiant phase transition. The dynamical nature of this cavity-induced synthetic magnetic field arises from the delicate interplay between collective superradiant scattering and the underlying fractal band structure. Using a sixth-order expansion of the free energy as a function of the order parameter and by numerical simulations, we show that at low magnetic fluxes the superradiant ordering phase transition is first order, while it becomes second order for higher flux. The dynamic nature of the magnetic field induces a nontrivial deformation of the Hofstadter butterfly in the superradiant phase. At strong pump far above the self-ordering threshold, we recover the Hofstadter butterfly one would obtain in a static magnetic field.

DOI: 10.1103/PhysRevB.100.224306

I. INTRODUCTION

In the last decade, advancements in the manipulation of cold atomic gases enabled the engineering of Hamiltonians emulating the physics of effective gauge fields [1,2]. The development of rotating traps [3,4] allowed to overcome the challenge of coupling the external degrees of freedom of neutral atoms to an effective vector gauge potential as for charged particles. More sophisticated techniques based on light-matter interaction [5,6] and lattice shaking [7,8] were also developed to imprint a position-dependent geometric phase onto the atomic wave function, analogous to the Aranov-Bohm phase of electrons in an external magnetic field [9]. Shortly after, the Hofstadter model [10,11] was implemented for cold atoms in optical lattices by employing a laser-assisted tunneling scheme [12–14]. The realization of such an artificial magnetic field in lattice geometries [15,16] allows one to explore the realm of topological many-body states of matter [17–19]. The most notable examples include measuring the Chern number of nontrivial topological bands [20] and realizing the Meissener phases for neutral atoms in ladder geometries [21]. More recently, techniques exploiting internal degrees of freedom as synthetic dimensions have been developed [22,23] and are candidates for the observation of the quantum Hall effect even in four dimensions [24].

The experimental realization of lattice models with effective gauge potential is of great interest for engineering synthetic gauge theories [25]. Experimental realizations have so far implemented static gauge fields which can be finely tuned by varying experimental parameters, but are not dynamically affected by the atomic back action. However, to simulate a genuine gauge theory, quantum matter needs to be dynamically coupled to a gauge (bosonic) field and the back action of the matter dynamics onto the gauge field should be accounted for. A first step in this direction is to use density-dependent synthetic gauge fields [26,27], which were recently observed for a Bose-Einstein Condensate (BEC) in a shaken optical lattice [28,29]. A Z_2 lattice gauge theory was also experimentally realized [30,31].

Optomechanical systems [32,33] as well as cold atoms in optical cavities [34] provide another natural route to the realization of a dynamical gauge theory in a controllable and accessible environment. This hinges on the nonlinearity of these systems, where photons (phonons) feel the back action of the atomic motion (photons). In view of the experimental realization of a strongly interacting Fermi gas coupled to a cavity [35] and the recent observation of a dynamical spin-orbit coupling in a BEC in a linear cavity [36–39], theoretical proposals [40–48] for dynamical gauge fields are now in reach by experiments.

Here we study dynamical cavity-supported synthetic magnetic fields for fermions in an external optical lattice [12]. Atoms are driven by two transverse counterpropagating lasers and can scatter photons into the cavity. The hopping along the cavity axis is suppressed by a potential gradient. By choosing proper laser detunings, it can be activated by resonant Raman scattering of pump photons into a single resonant standing-wave mode of the cavity [47]. Each pump laser here is responsible for a particular hopping direction. Above a critical pump strength, the collective buildup of the cavity field enables resonant coherent tunneling. In addition, for any closed loop in the atomic trajectory, a geometric phase proportional to the enclosed area is imprinted onto the atomic wave function, in analogy to the phase acquired by electrons in a magnetic field.

The onset of the superradiant (SR) phase transition and the appearance of a synthetic magnetic field depends strongly on

---

[*] elvia.colella@uibk.ac.at

the phases imprinted, which can be tuned by setting the ratio between the lattice constant and the pump field wavelength $B \propto d_y/\lambda_c$. This is due to an intricate interplay between SR scattering generating the synthetic magnetic field and the emerging fractal energy bands corresponding to this field. Such cavity-induced atomic back action on the effective gauge potential is very different from existing free-space implementations. Interestingly, as shown below, the onset of the SR phase transition (and hence appearance of the synthetic magnetic field) exhibits a first-order behavior at low fluxes, where the energy bands are Landau-like, while it becomes second order for high flux. The energy spectrum itself carries the signs of the nonlinearity of the atom-light interactions and the dynamical nature of the magnetic field, resulting in the emergence of peculiar structures compared to the commonly known energy spectrum, i.e., Hofstadter butterfly [11].

The paper is organized as follows. In Sec. III D, we introduce the detailed system model. The physical results are summarized in Sec. III, where we focus on the bulk properties of the system at half filling. Here the gas behaves as a metal or semimetal, depending on the value of the magnetic flux in a plaquette. We show the phase diagram, the energy spectrum, and we investigate the point of change of the phase transition from first to second order. Our final considerations are reported in Sec. IV.

II. MODEL

We consider a Fermi gas confined in a two-dimensional (2D) optical lattice of a lattice constant, $\mathbf{d} = \{d_x, d_y\}$, in the tight-binding regime. Hopping in the x direction is suppressed by an additional energy gradient $\hbar\Delta$ between neighboring sites. This can be realized by adding a constantly accelerated optical lattice, a magnetic field, or an electric field gradient along the x direction. We consider only a single internal atomic transition $|g\rangle \leftrightarrow |e\rangle$ of frequency ω_0. The hopping in the x direction is restored via two-photon resonant scattering processes mediated by cavity photons, where the resonance condition is $\omega_c \simeq \omega_1 + \Delta = \omega_2 - \Delta$ [12]. Here, ω_1 and ω_2 are the frequencies of the two transversal laser pumps; see Fig. 1.

Our model Hamiltonian in a tight-binding approximation in a reference frame rotating at the average pump frequency $\omega_p = (\omega_1 + \omega_2)/2$ then reads [47]

$$\begin{aligned} H = &- J_y \sum_{l,m} (f^\dagger_{l,m+1} f_{l,m} + \text{H.c.}) \\ &- \hbar\eta(a + a^\dagger) \sum_{l,m} (e^{2i\pi m\gamma} f^\dagger_{l+1,m} f_{l,m} + \text{H.c.}) \\ &- \hbar\Delta_c a^\dagger a. \end{aligned} \tag{1}$$

Here J_y is the hopping amplitude in the y direction, $\eta = \Omega_1 g_0/\delta = \Omega_2 g_0/\delta$ is the two-photon Rabi coupling with $\delta = \omega_p - \omega_0$ the atomic detuning with respect to the average pump frequency, g_0 is the bare coupling strength of the cavity mode to the atomic transition and $\Delta_c = \omega_p - \omega_c$ is the cavity detuning with respect to the average pump ω_p. Note that only resonant Raman scattering terms are retained in the Hamiltonian. Further details are presented in Appendix A.

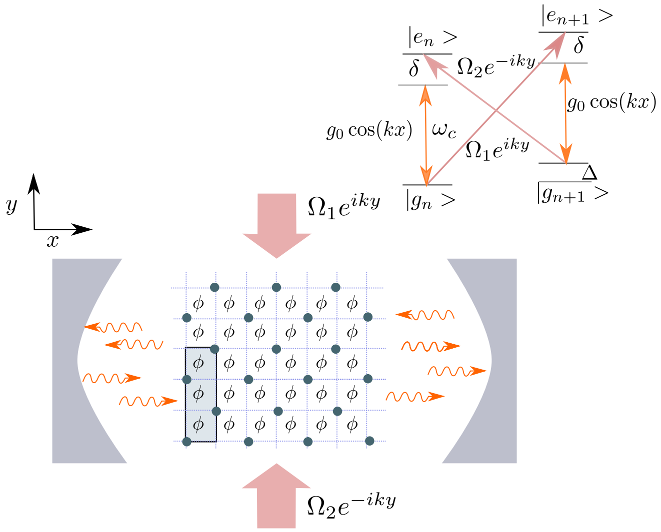

FIG. 1. Geometry sketch to realize a dynamical version of the Harper-Hofstadter Hamiltonian: A 2D Fermi gas in a rectangular lattice within a single-mode optical cavity is transversely illuminated by two counterpropagating laser beams of orthogonal polarization. The shaded area in the lattice represents the unit cell for $\phi = 2\pi/3$.

The spatial phase dependence of the pump lasers imprints a site-dependent tunneling phase $\gamma_m = m\gamma = mk_L/(2\pi/d_y)$. Hence, hopping around a plaquette, the wave function acquires a total phase $\phi = 2\pi\gamma$, which can be related to an electron moving in a periodic potential threaded by a magnetic field of strength $|B| = 2\pi\gamma/(d_y^2 e)$.

The effective magnetic field breaks the translation symmetry of the original lattice and the Hamiltonian is invariant under a combination of discrete translation and a gauge transformation, i.e., magnetic translation. In particular, when $\gamma = p/q$ is a rational number with p and q being two integers, and the energy spectrum splits into q subbands, which cluster in a highly fractal structure known as Hofstadter butterfly [11].

In contrast to free-space setups, the hopping amplitude in the cavity direction depends on the cavity field amplitude and the effective magnetic field appears only for the nonzero cavity field. Here the coherent amplitude $\langle a\rangle = \alpha$ is determined by the steady-state solution of the mean-field equation,

$$\frac{\partial\alpha}{\partial t} = -(\Delta_c - i\kappa)\alpha - \eta\Theta = 0, \tag{2}$$

where

$$\Theta = \sum_{l,m} (e^{-2i\pi\gamma m}\langle f^\dagger_{l,m} f_{l-1,m}\rangle + e^{2i\pi\gamma m}\langle f^\dagger_{l,m} f_{l+1,m}\rangle) \tag{3}$$

is the atomic order parameter, which reveals emergent currents of equal number of left- and right-moving atoms along the cavity axis. The order parameter Θ needs to be self-consistently determined by diagonalizing the Hamiltonian at fixed amplitude α:

$$\Theta = \frac{2}{N_k^2} \sum_m \sum_{s=1}^{q} \sum_{\mathbf{k}\in\text{B.Z.}} n_F(\epsilon_{s,\mathbf{k}}) \cos(2\pi m\gamma) |v_{s,\mathbf{k}}(m)|^2. \tag{4}$$

Here $\epsilon_{s,\mathbf{k}}$ and $v_{s,\mathbf{k}}(m)$ are the eigenvalues and eigenstates of the Harper equation [10]:

$$J_y[e^{ik_y}w_{\mathbf{k}}(m+1)+e^{-ik_y}w_{\mathbf{k}}(m-1)] \\ +2\eta(\alpha+\alpha^*)\cos(k_x-2\pi m\gamma)w_{\mathbf{k}}(m)=\epsilon w_{\mathbf{k}}(m). \quad (5)$$

We use the following Ansatz for the atomic wave function $\Psi(l,m)=e^{ik_xl}e^{ik_ym}w_{\mathbf{k}}(m)$, with $w_{\mathbf{k}}=\sum c_s v_{s,\mathbf{k}}(m)$ a linear superposition of the eigenstates of the Hamiltonian.

Equations (4) and (5) are solved self-consistently within the reduced Brillouin zone $k_x\in[-\pi,\pi]$ and $k_y\in[-\pi/q,\pi/q]$, for a magnetic unit cell with periodic boundary conditions in x and y directions. We focus on the contribution of the bulk to the superradiance, neglecting boundary effects which appear in a pair of chiral edge states [47].

III. RESULTS

A. Phase diagram

For weak pump $\eta\sqrt{N}$, the system is in the uncoupled normal state (N), i.e., the atoms form a collection of independent chains in the y direction and the cavity is empty. Increasing the effective pump strength the system exhibits a transition to a SR state, where photons are resonantly scattered into the cavity mode and the hopping in the cavity (x) direction builds up.

The stationary cavity-field amplitude is depicted in Fig. 2. It grows continuously above the SR threshold for large magnetic flux ($0.21<\gamma<0.5$) but displays a noncontinuous jump at lower $\gamma<0.21$. To better understand the change from a second- to a first-order phase transition, as presented in Appendix B, we expand the free energy of the system in the Landau form up to sixth order in the atomic order parameter:

$$F\sim\left(1-\frac{4\Delta_c}{\Delta_c^2+\kappa^2}\chi_1\eta^2\right)|\Theta|^2-\frac{8\Delta_c^3}{\left(\Delta_c^2+\kappa^2\right)^3}\chi_3\eta^6|\Theta|^4 \\ -\frac{64\Delta_c^5}{3\left(\Delta_c^2+\kappa^2\right)^5}\chi_5\eta^{10}|\Theta|^6. \quad (6)$$

The effective optical response of the Fermi gas after cycles of absorption and emission of cavity photons is determined by the static susceptibilities, χ_i (Fig. 3). The linear susceptibility χ_1 determines the phase transition threshold,

$$\sqrt{N}\eta_c=\sqrt{\frac{\Delta_c^2+\kappa^2}{4\Delta_c\chi_1}N}, \quad (7)$$

which is shown as a red solid line in Fig. 2. The sign of χ_3 determines the order of the phase transition.

In particular, for strong magnetic fields we have $\chi_3>0$ and the transition is of the second order. The atoms then behave like a Kerr medium [49], inducing an intensity-dependent shift of the refractive index, $n=n_0+n_2I$, with $n_2=-8\chi_3\eta^2\Delta_c^3(\Delta_c^2+\kappa^2)$. For decreasing magnetic field, the third-order susceptibility monotonically decreases, becoming negative at $\gamma\simeq 0.21$, which renders the transition first order (bottom panel of Fig. 3). In this regime, higher order susceptibilities only slightly depend on the magnetic flux γ. In fact, the atomic orbit size significantly exceeds the unit cell of the original lattice, making the lattice structure negligible.

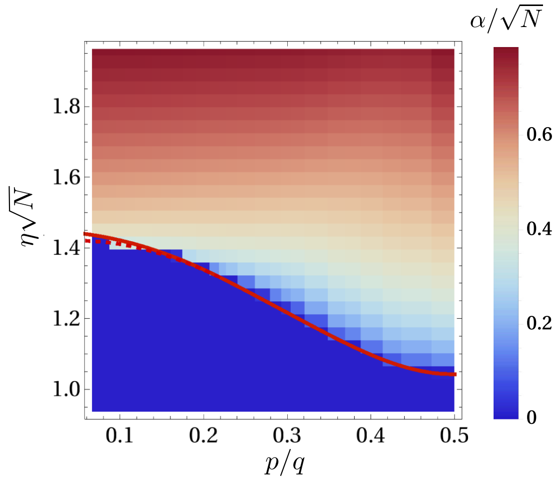

FIG. 2. Phase boundary (red line) as function of effective flux $\gamma/2\pi=p/q$ and rescaled pump field $\eta\sqrt{N}$ using the field amplitude modulus $|\alpha|/\sqrt{N}$ as background color. Note that p/q is discrete and rational, with $1<p<7$ and $1<q<15$. The field amplitude is determined self-consistently for a Fermi gas at half-filling at fixed finite temperature $k_BT=0.5E_R$, where $E_R=\hbar^2k_c^2/2m$ is the recoil energy. At small fluxes, $\gamma<0.21$, the system exhibits a first-order phase transition, while for bigger fluxes it is of second order. The solid red line shows the analytical result for the critical threshold and the red dashed line the beginning of the region of hysteresis.

The system then exhibits a universal behavior and the band structure corresponds to Landau levels in free space.

B. First-order transition

At low γ, the emergent magnetic field has only a little influence on the system dynamics. The temperature and the presence of an open Fermi surface then play a fundamental role to unravel the physical origin of the first-order behavior of the phase transition. By inspection of the temperature

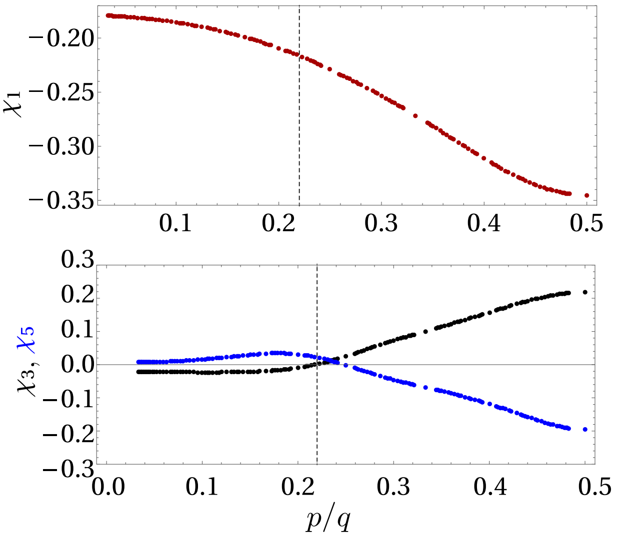

FIG. 3. Atomic susceptibilities, χ_1 (red), χ_3 (black), and χ_5 (blue) at $k_bT=0.5E_R$. The third order susceptibility χ_3 becomes negative below $p/q=0.21$, signaled by the dashed black line.

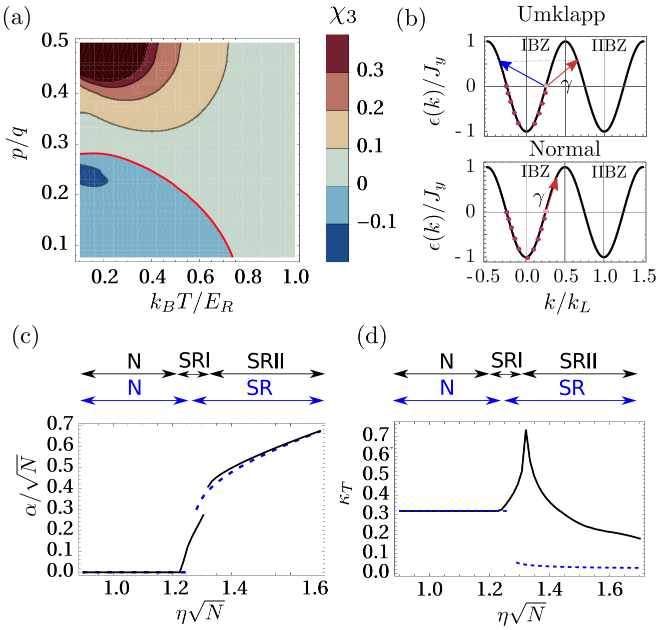

FIG. 4. (a) Third-order susceptibility, χ_3, as a function of the temperature and effective magnetic flux, $2\pi\gamma = 2\pi p/q$, with $1 < p < 6$ and $1 < q < 13$. The red line corresponds to zero susceptibility, separating positive and negative regions. (b) An atom at the Fermi surface is scattered after absorbing a photon to a higher energy state via an Umklapp (top panel) or a normal process (bottom panel). The process is depicted using two Brillouin zones of the original lattice. Cavity field amplitude (c) and isothermal compressibility (d) at $k_bT = 0.05E_R$ for $\gamma = 1/3$ (solid black) and $\gamma = 1/4$ (dashed blue).

dependence of χ_3 for a Fermi gas at half filling, we can identify an important change around $\gamma \approx k_F/k_L = 1/4$ [Fig. 4(a)]. The susceptibility χ_3 is either positive at any temperature or becomes negative at low temperature. The two regions are separated by the red solid line in Fig. 4(a).

In the latter case, the phase transition becomes first order at low temperatures. This coincides with the regime where scattering one photon keeps the atomic momentum state within the same first Brillouin zone of the original lattice (normal scattering). In contrast, the transition becomes second order when the photon scattering is an Umklapp process [Fig. 4(b)], i.e., by inverting the direction of the atomic motion, a momentum transfer ($G = nk_L$) to the optical lattice is required. However, the occupation of higher energy states at higher temperatures can favor the Umklapp processes at the expense of direct scattering, enhancing the rate to scatter to the next Brillouin zone even for a small momentum transfer. This explains why at higher temperatures a second-order phase transition occurs and the critical temperature at which this happens increases for small γ [Fig. 4(a)].

These results are confirmed by the numerical simulations at lower temperatures, $k_bT = 0.05E_R$. The rescaled cavity amplitude as a function of the pump strength either grows continuously around the threshold for $\gamma = 1/3$ [black line in Fig. 4(c)] or exhibits a jump at the critical point for $\gamma = 1/4$ [blue dashed line in Fig. 4(c)]. For $\gamma = 1/3$, the rescaled amplitude shows an additional jump at higher pumps $\eta > \eta_c$, hinting that an additional first-order transition inside the SR phase can appear. Such transition occurs when the cavity-induced hopping exceeds the hopping in the y direction, $J_x/J_y = \eta(\alpha + \alpha^*) = 1$. The two SR states are characterized by the same order parameter but different isothermal compressibility, $\kappa_T = (1/\rho^2)\partial\rho/\partial\mu$, where ρ is the density of the Fermi gas. This divides the SR region into two phase zones: SRI and SRII. In many respects, this suggests a liquid-gas type of transition between the SRI and SRII phases, as confirmed by the rapid growth of density fluctuations that can be inferred from the divergence of the compressibility at the critical point [Fig. 4(d)]. The transition is reminiscent of the case observed for fermions in linear cavities without external optical lattice [50]. In the latter case, however, the transition was driven by the coupling to an additional degree of freedom, in a process similar to the Larkin-Pimkin mechanism [51].

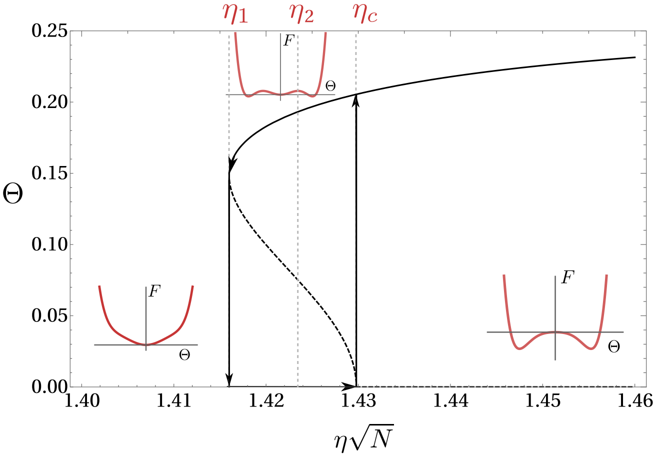

FIG. 5. Atomic order parameter at $T = 0.5E_R$ for $\gamma = 1/12$ as a function of the effective pump $\eta\sqrt{N}$. The arrows shows the hysteresis loop and the dotted lines represent the metastable solution. The insets show a qualitative picture of the free energy in the different regimes.

C. Hysteresis

For small magnetic flux, the system exhibits a bistable hysteresis behavior near the SR threshold η_c. The hysteresis loop and a qualitative picture of the free energy in the different regions are shown in Fig. 5. As can be seen in the insets, below the threshold

$$\eta_1 = \frac{\eta_c}{\sqrt{1 - \chi_3^2/(12\chi_1\chi_5)}}, \tag{8}$$

the solution with $\alpha = 0$ (empty cavity) is the only minimum of the free energy. Between $\eta_1 < \eta < \eta_c$, the free energy has three minima, either local or absolute. The solution for $\alpha \neq 0$ is metastable for $\eta_1 < \eta < \eta_2$, with

$$\eta_2 = \frac{\eta_c}{\sqrt{1 - 3\chi_3^2/(8\chi_1\chi_5)}}. \tag{9}$$

Between $\eta_2 < \eta < \eta_c$, the zero field solution $\alpha = 0$ is metastable and finally ceases to be a minimum at η_c, where the system becomes SR.

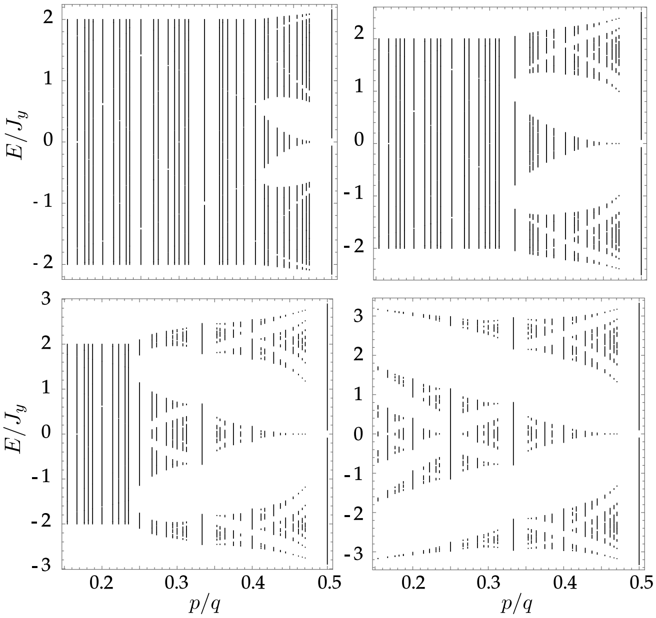

FIG. 6. Energy spectrum as function of flux p/q for four different pump strengths $\eta\sqrt{N} = \{1.1, 1.2, 1.3, 1.4\}E_R$ from top left to bottom right corner at $k_bT = 0.5E_R$. The spectrum initially shows singular shapes and reduces to the conventional Hofstadter butterfly at strong pump.

D. Dynamical Hofstadter Butterfly

Figure 6 shows the energy spectrum as a function of the magnetic flux p/q for increasing pump strength $\eta\sqrt{N}$. The magnetic field, $B \sim p/q$, emerges spontaneously with the cavity field amplitude and leads to the opening of $q-1$ gaps in the band structure. As the SR phase is already entered at lower pump power for stronger magnetic fields, the gap opening progressively extends toward $p/q = 0$ as the pump is increased. The different structures visible in the energy spectrum strongly depend on the pump strength. At low pump strength (top panels of Fig. 6), the gaps organize in the shape of a small butterfly confined in the region of large magnetic fields $0.21 < \gamma < 0.5$. The gaps close at the boundary of this region, where the amplitude of the cavity field is infinitesimally small. When the pump is increased, the Hofstadter butterfly is entirely retrieved (right-bottom panel in Fig. 6) like in a static optical lattice. The gaps will gradually close, generating a 1D tight-binding in the x direction with bandwidth, $2J_x = 2\eta(\alpha + \alpha^*)$. In fact, the system evolves toward a regime of very weakly coupled 1D chains in the x direction, for which the magnetic field can be gauged out.

The distortion of the energy spectrum, compared to the conventional Hofstadter butterfly [11], is due to the dynamical nature of the coupling between atoms and cavity photons. At a fixed magnetic field, the system spontaneously chooses the most favorable amplitude of the cavity field, i.e., the effective hopping parameter, $J_x = \eta(\alpha + \alpha^*)$. As the system becomes SR, the effective Lorentz force exerted by the artificial magnetic field favors the tunneling in the x direction, resulting in an asymmetry of the tunneling amplitudes. Therefore, the energy spectrum can be seen as the superposition of different Hofstadter butterflies with asymmetric hopping, $J_x - J_y$. While the fractal structure is preserved by the form of the Hamiltonian as the hopping phase is not cavity dependent, the size of the gaps are set by the ratio of the hopping parameters and are characterized by a nontrivial dependence on the magnetic flux $2\pi p/q$.

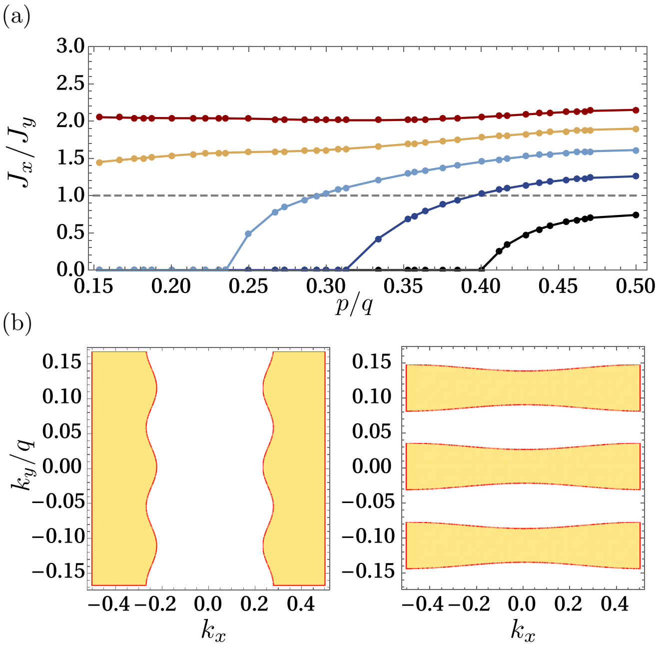

FIG. 7. (a) Effective cavity-induced hopping as a function of flux p/q at different pumping strengths. Parameters: $\eta\sqrt{N} = \{1.1, 1.2, 1.3, 1.4, 1.5\}E_R$ in black, dark blue, light blue, yellow, and red, respectively. (b) Fermi surface at $\gamma = 1/3$ for $k_bT = 0.5E_R$ for $\eta\sqrt{N} = 1.2E_R$ (left) and $\eta\sqrt{N} = 1.3E_R$ (right).

This is illustrated in Fig. 7(a), where the hopping ratio J_x/J_y is shown as a function of the magnetic flux for different pump strengths. In the weak pump regime (black and dark blue lines), the dynamic butterfly is a superposition of static Hofstadter butterflies with very different effective hopping amplitudes. The hopping in the x direction grows as the magnetic field is increased but remains rather small compared to the hopping in the other direction. As a consequence, the curvature of the band structure and the Fermi surface align along the y direction, see left panel in Fig. 7(b).

As the pump is increased, the field amplitude and the hopping in the x direction become almost independent of the magnetic flux [red and yellow line in Fig. 7(a)]. In this regime, the kinetic energy in the x direction dominates and the Fermi surface aligns along the cavity axis. Note that at low temperature, this is accompanied by the onset of a first-order transition within the SR phase, SRI-SRII, as shown in the previous section.

IV. CONCLUSIONS AND OUTLOOK

We have shown that nonlinear coupling between atomic motion and a cavity-field mode offers a perspective on the generation of synthetic dynamical magnetic fields. In contrast to free space, the gauge field emerges spontaneously via maximizing the light scattered into the cavity and changing the atomic density configuration. The complex interplay between

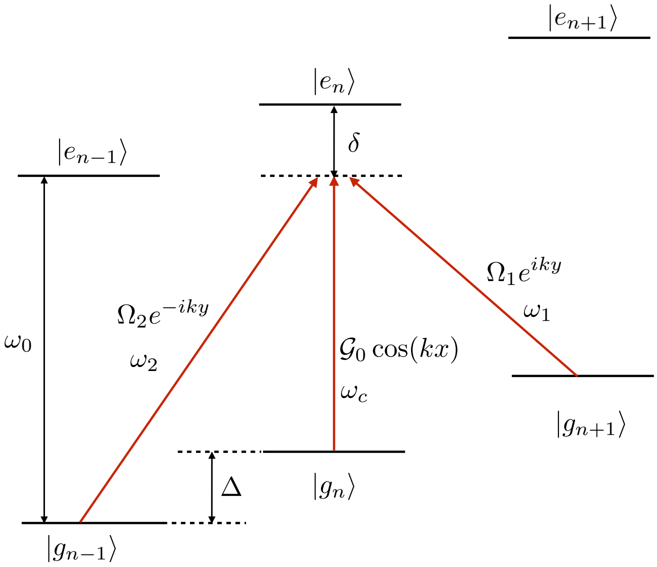

FIG. 8. Three generic lattice sites along x direction.

the fractal structure of the energy bands and the SR scattering thus generates shapes for a dynamical Hofstadter butterfly.

Note that atoms are coupled only to a specific wavelength of the light field determined by the chosen cavity mode. As shown recently, employing several distinct cavity modes the system gets more freedom and a global symmetry can "emerge" in a cavity-QED system [52]. Therefore, generalization of our studied system to multimode cavities and, in particular, a ring or fiber geometry [53] could allow us to fully reproduce the minimal coupling of a charged particle to a local $U(1)$ gauge potential. Making use of the dynamical coupling between light and atoms in cavity systems is a promising route toward the experimental realization of synthetic dynamical gauge fields. Moreover, on a different level, the mediation of long-range two-body interactions due to the exchange of photons can lead to the observation of exotic states, such as particles with anyonic statistics in fractional quantum Hall states.

ACKNOWLEDGMENTS

F.M. is grateful to N. Goldman for fruitful discussions. F.M. is supported by the Lise-Meitner Fellowship M2438-NBL of the Austrian Science Fund (FWF), and the International Joint Project No. I3964-N27 of the FWF and the National Agency for Research (ANR) of France.

APPENDIX A: EFFECTIVE HAMILTONIAN

Consider atoms loaded into a 2D optical lattice of lattice constant, $\mathbf{d} = [d_x, d_y]$. The hopping along x direction is at first suppressed due to the potential offset Δ between adjacent lattice sites and then restored thanks to the cavity- and laser-assisted hoppings. The hopping along y direction is due to the kinetic energy of the atoms. Let us just focus on the x direction and consider three generic lattice sites labeled $n-1$, n, and n as in Fig. 8. First consider only transitions which involve the atomic excited state in site n, that is, $|e_n\rangle$. The Hamiltonian $H = H_0 + H_{\mathrm{int}}$ reads ($\hbar = 1$),

$$H_0 = -(\omega_0 + \Delta)\sigma_{n-1} - \omega_0\sigma_n - (\omega_0 - \Delta)\sigma_{n+1} + \omega_c a^\dagger a, \tag{A1}$$

$$\begin{aligned} H_{\mathrm{int}} = {} & \Omega_2 e^{-iky} e^{-i\omega_2 t}\sigma^+_{n-1} + g_0\cos(kx_n)a\sigma^+_n \\ & + \Omega_1 e^{iky} e^{-i\omega_1 t}\sigma^+_{n+1} + \mathrm{H.c.}, \end{aligned} \tag{A2}$$

where $\sigma_{n-1} = |g_{n-1}\rangle\langle g_{n-1}|$, $\sigma_n = |g_n\rangle\langle g_n|$, $\sigma_{n+1} = |g_{n+1}\rangle\langle g_{n+1}|$, $\sigma^+_{n-1} = |e_n\rangle\langle g_{n-1}|$, $\sigma^+_n = |e_n\rangle\langle g_n|$, $\sigma^+_{n+1} = |e_n\rangle\langle g_{n+1}|$. For simplicity a two-photon resonance is assumed $\omega_c = \omega_1 + \Delta = \omega_2 - \Delta$ in the following and $k \equiv k_c \simeq k_1 \simeq k_2$.

Applying the unitary transformation $U = \exp\{-i[\omega_2\sigma_{n-1} + \omega_p(\sigma_n - a^\dagger a) + \omega_1\sigma_{n+1}]t\}$ to the Hamiltonian H yields

$$\begin{aligned} \tilde{H} = {} & \delta(\sigma_{n-1} + \sigma_n + \sigma_{n+1}) + [\Omega_2 e^{-iky}\sigma^+_{n-1} \\ & + g_0\cos(kx_n)a\sigma^+_n + \Omega_1 e^{iky}\sigma^+_{n+1} + \mathrm{H.c.}], \end{aligned} \tag{A3}$$

where $\delta = \omega_c - \omega_0 \sim \omega_p - \omega_0$, with $\omega_p = (\omega_1 + \omega_2)/2$ the average pump frequency. Here we have made use of the relations $U\sigma^+_{n-1}U^\dagger = e^{i\omega_2 t}\sigma^+_{n-1}$, etc. and $\tilde{H} = UHU^\dagger + i(\partial_t U)U^\dagger$. We find the stationary values of the operators σ^+_{n-1}, σ^+_n, σ^+_{n+1} by setting to zero the Heisenberg equation of motion $i\partial_t O = [O, \tilde{H}]$ upon assuming a large detuning δ,

$$\begin{aligned} \sigma^+_{n-1} \simeq {} & \frac{1}{\delta}(\Omega_2^* e^{iky}\sigma_{n-1} + \Omega_1^* e^{-iky}\sigma_{n+1,n-1} \\ & + g_0\cos(kx_n)a^\dagger\sigma_{n,n-1}), \\ \sigma^+_n \simeq {} & \frac{1}{\delta}(\Omega_2^* e^{iky}\sigma_{n-1,n} + \Omega_1^* e^{-iky}\sigma_{n+1,n} \\ & + g_0\cos(kx_n)a^\dagger\sigma_n), \\ \sigma^+_{n+1} \simeq {} & \frac{1}{\delta}(\Omega_2^* e^{iky}\sigma_{n-1,n+1} + \Omega_1^* e^{-iky}\sigma_{n+1} \\ & + g_0\cos(kx_n)a^\dagger\sigma_{n,n+1}), \end{aligned} \tag{A4}$$

where $\sigma_{n,n-1} = |g_n\rangle\langle g_{n-1}|$, $\sigma_{n+1,n-1} = |g_{n+1}\rangle\langle g_{n-1}|$, $\sigma_{n+1,n} = |g_{n+1}\rangle\langle g_n|$, etc. Here we have also assumed a negligible population of the excited state, $|e_n\rangle\langle e_n| \simeq 0$, due to the large detuning δ.

Substituting Eq. (A4) back in the Hamiltonian Eq. (A3) yields the effective Hamiltonian,

$$\begin{aligned} \tilde{H}^{(n)}_{\mathrm{eff}} = {} & \frac{2}{\delta}\{g_0^2\cos^2(kx_n)a^\dagger a\sigma_n \\ & + [\Omega_2 g_0 e^{-iky}\cos(kx_n)a^\dagger\sigma_{n,n-1} \\ & + \Omega_1^* g_0 e^{-iky}\cos(kx_n)a\sigma_{n+1,n} + \mathrm{H.c.}]\}, \end{aligned} \tag{A5}$$

where the constant terms proportional to Ω_1 and Ω_2, and terms involving next-nearest-neighbor scattering $\sigma_{n+1,n-1}$ have been omitted.

Considering now transitions which involve the states $|e_{n\pm1}\rangle$ results in the following contributions to the $\{n-1, n, n+1\}$ manifold:

$$\begin{aligned} \tilde{H}^{(n-1)}_{\mathrm{eff}} \propto {} & \frac{2}{\delta}\{g_0^2\cos^2(kx_{n-1})a^\dagger a\sigma_{n-1} \\ & + [\Omega_1^* g_0 e^{-iky}\cos(kx_{n-1})a\sigma_{n,n-1} + \mathrm{H.c.}]\}, \end{aligned}$$

$$\tilde{H}_{\text{eff}}^{(n+1)} \propto \frac{2}{\delta}\big\{g_0^2\cos^2(kx_{n+1})a^\dagger a\sigma_{n+1} + \big[\Omega_2 g_0 e^{-iky}\cos(kx_{n+1})a^\dagger\sigma_{n1,n} + \text{H.c.}\big]\big\}. \tag{A6}$$

Assuming $\Omega_1 = \Omega_2 = \Omega \in \mathbf{R}$ and $\lambda_c = 2\pi/k = d_x$, the total effective Hamiltonian takes the form

$$\tilde{H}_{\text{eff}} = \frac{2}{\delta}\sum_n \big\{g_0^2\cos^2(kx_n)a^\dagger a\sigma_n + \Omega g_0(a+a^\dagger)[e^{-iky}\cos(kx_n)\sigma_{n,n-1} + \text{H.c.}]\big\}, \tag{A7}$$

or in the second-quantized tight-binding formalism,

$$\begin{aligned}\tilde{H}_{\text{eff}} =& a^\dagger a\sum_{n,m}\epsilon_{n,m}c^\dagger_{n,m}c_{n,m} \\ &+ (a+a^\dagger)\sum_{n,m}\big(J^x_{n,m}e^{-iky_m}c^\dagger_{n,m}c_{n-1,m} + \text{H.c.}\big) \\ &+ J^y\sum_{n,m}(c^\dagger_{n,m}c_{n,m-1} + \text{H.c.}),\end{aligned} \tag{A8}$$

where the hopping along the y direction is now also included. The matrix elements are given by

$$\begin{aligned}\epsilon_{n,m} &= \frac{2}{\delta}g_0^2\iint dxdy\cos^2(kx)|W(x-x_n)W(y-y_n)|^2 \\ &= \frac{2}{\delta}g_0^2\iint dx\cos^2(kx)|W(x-x_n)|^2, \\ J^x_{n,m}e^{-iky_m} &= \frac{2}{\delta}\Omega g_0\iint dxdyW^*(x-x_n)W^*(y-y_n) \\ &\quad\times e^{-iky}\cos(kx)W(x-x_{n-1})W(y-y_m) \\ &= \frac{2}{\delta}\Omega g_0\int dx\cos(kx)W^*(x-x_n)W(x-x_{n-1}) \\ &\quad\times\int dye^{-iky}W^*(y-y_m)W(y-y_m),\end{aligned} \tag{A9}$$

where $W(\mathbf{X}-\mathbf{R}) = W(x-x_n)W(y-y_m)$ is the ground-state Wannier function describing particles localized at the site $[n, m]$.

APPENDIX B: FREE-ENERGY EXPANSION

To derive an effective Landau theory for the atomic order parameter Θ, as defined in the main text, we start from the the action of the system expressed in momentum space:

$$\begin{aligned}&S[\alpha,\alpha^*,c^\dagger_{k_x,k_y},c_{k_x,k_y}] \\ &= \Delta_c|\alpha|^2 \\ &\quad+\frac{1}{\beta V}\sum_{n,k_x,k_y}(i\omega_n - 2J_y\cos(k_y))c^\dagger_{n,k_x,k_y}c_{n,k_x,k_y} \\ &\quad-\eta(\alpha+\alpha^*)\frac{1}{\beta V}\sum_{k_x,k_y}\big(e^{-k_x}c^\dagger_{k_x,k_y}c_{k_x,k_y+\gamma} \\ &\quad+e^{-k_x}c^\dagger_{k_x,k_y}c_{k_x,k_y-\gamma}\big).\end{aligned} \tag{B1a}$$

Note that only the static component of the bosonic field α is retained, which is linearly related to the atomic order parameter by the equation of motion $\alpha = -\eta\Theta/(\Delta_c - i\kappa)$. We integrate out fermionic degrees of freedom, obtaining an effective action for the photonic field only, $S_{\text{eff}}[\alpha,\alpha^*] = \Delta_c|\alpha|^2 + \text{tr }\ln\hat{\text{G}}^{-1}$. The trace operator

$$\text{tr }\ln\hat{\text{G}}^{-1} = \text{tr }\ln\text{G}_0^{-1} - \sum_{\text{n}}\frac{1}{2\text{n}}\text{tr}(\text{G}_0\Gamma)^{2\text{n}} \tag{B2}$$

is obtained by perturbatively expanding the Green function $G(\mathbf{k}, i\omega_n)$ around the zero order one,

$$G_0^{-1}(\mathbf{k},\omega_n) = \begin{bmatrix}\ddots & 0 & 0 & 0 & 0 \\ 0 & i\omega_n - 2J_y\cos(k_y-\gamma) & 0 & 0 & 0 \\ 0 & 0 & i\omega_n - 2J_y\cos(k_y-\gamma) & 0 & 0 \\ 0 & 0 & 0 & i\omega_n - 2J_y\cos(k_y-\gamma) & 0 \\ 0 & 0 & 0 & 0 & \ddots\end{bmatrix}, \tag{B3}$$

where the perturbative term is given by the interaction matrix

$$\Gamma(\mathbf{k}) = -\eta(\alpha+\alpha^*)\begin{bmatrix}0 & e^{-ik_x} & 0 & 0 & 0 \\ e^{ik_x} & 0 & e^{-ik_x} & 0 & 0 \\ 0 & e^{ik_x} & 0 & e^{-ik_x} & 0 \\ 0 & 0 & e^{ik_x} & 0 & e^{-ik_x} \\ 0 & 0 & 0 & e^{ik_x} & 0\end{bmatrix}. \tag{B4}$$

Here, $i\omega_n = \pi(2n+1)/\beta$ are fermionic Matsubara frequencies. By keeping up to the sixth order in α, the effective free energy is

$$\begin{aligned}F =& \Delta_c|\alpha|^2 - \eta^2\chi_1(\alpha+\alpha^*)^2 - \frac{\eta^4}{2}\chi_3(\alpha+\alpha^*)^4 \\ &- \frac{\eta^6}{3}\chi_5(\alpha+\alpha^*)^6,\end{aligned} \tag{B5}$$

or in powers of the atomic order parameter, Θ, reads

$$\begin{aligned}F \sim& \left(1 - \frac{4\Delta_c}{\Delta_c^2+\kappa^2}\chi_1\eta^2\right)|\Theta|^2 - \frac{8\Delta_c^3}{(\Delta_c^2+\kappa^2)^3}\chi_3\eta^6|\Theta|^4 \\ &- \frac{64\Delta_c^5}{3(\Delta_c^2+\kappa^2)^5}\chi_5\eta^{10}|\Theta|^6.\end{aligned} \tag{B6}$$

The free energy depends on the cavity properties and the coupling with the atoms is enclosed inside the susceptibilities

$$\chi_1 = \frac{1}{\beta}\sum_{n,k\in \mathrm{BZ}} G_k(i\omega_n)G_{k+\gamma}(i\omega_n), \tag{B7a}$$

$$\chi_3 = \frac{1}{\beta}\sum_{n,k\in \mathrm{BZ}} \big[G_k^2(i\omega_n)G_{k+\gamma}^2(i\omega_n) + 2G_{k-\gamma}(i\omega_n)G_k^2(i\omega_n)G_{k+\gamma}(i\omega_n)\big], \tag{B7b}$$

$$\chi_5 = \frac{1}{\beta}\sum_{n,k\in \mathrm{BZ}} \big[G_k^3(i\omega_n)G_{k+\gamma}^3(i\omega_n) + 3G_{k-\gamma}^2(i\omega_n)G_k^3(i\omega_n)G_{k+\gamma}(i\omega_n) + 3G_{k-\gamma}(i\omega_n)G_k^3(i\omega_n)G_{k+\gamma}^2(i\omega_n) + 3G_k(i\omega_n)G_{k+\gamma}^2(i\omega_n)G_{k+2\gamma}^2(i\omega_n)G_{k+3\gamma}(i\omega_n)\big]. \tag{B7c}$$

The susceptibilities shown in the main text are numerically calculated by truncating the summation over the Matsubara frequencies until convergence with fixed chemical potential $\mu = 0$, the same for the matrices $G_0(\mathbf{k}, \omega_n)$ and $\Gamma(\mathbf{k})$, which are summed in momentum space over the original Brillouin zone $[-\pi/d_x, \pi/d_y]$.

Expansion of the susceptibility for low magnetic fluxes

To have a better understanding of the physics at low magnetic fluxes, we have analytically computed the expressions for the susceptibilities χ_1 and χ_3. The first-order susceptibility is

$$\chi_1 = \sum_{k\in \mathrm{BZ}} \frac{n_F(\epsilon_{k+\gamma}) - n_F(\epsilon_k)}{\epsilon_{k+\gamma} - \epsilon_k}, \tag{B8}$$

with $\epsilon_k = J_y \cos(k)$, the tight-binding energy along the y direction where we set $\mu = 0$ for half filling. We expand χ_1 for small γ:

$$\chi_1(\gamma \ll 1) = \sum_{k\in \mathrm{BZ}} [-\beta n_F(\cos(k))[1 - n_F(\cos(k))]]. \tag{B9}$$

Note that the linear term vanishes and the main contribution to the linear susceptibility is a constant, which is proportional to the compressibility of a 1D chain of fermionic particles in the tight-binding regime. As $n_F(\epsilon)$ is the probability that the state ϵ is occupied, while $1 - n_F(\epsilon)$ is the probability that the state ϵ is not occupied, their product represents the scattering amplitude of a scattering process between two states of the same energy, which at very low temperature is only possible from one side to the other of the Fermi surface. The next contribution to χ_1 is quadratic and this behavior can also be observed in the plot of the susceptibility χ_1, see Fig. 2 in the main text. Note that at zero order, in γ we don't see the effect of the magnetic field but rather the temperature, dimensionality, and filling play the fundamental role.

The third-order χ_3 susceptibility represents the response of the medium to three photon processes, through cycles of multiple emission and absorption. The full analytics expression is

$$\begin{aligned}\chi_3 = \sum_{k\in \mathrm{BZ}} &-2\frac{n_F(\epsilon_{k+\gamma}) - n_F(\epsilon_k)}{(\epsilon_{k+\gamma} - \epsilon_k)^3} \\ &+ \frac{n_F'(\epsilon_{k+\gamma}) - n_F'(\epsilon_k)}{(\epsilon_{k+\gamma} - \epsilon_k)^2} \\ &+ 2\frac{n_F(\epsilon_{k-\gamma})}{(\epsilon_{k-\gamma} - \epsilon_k)^2(\epsilon_{k-\gamma} - \epsilon_{k+\gamma})} \\ &- 2\frac{n_F(\epsilon_{k+\gamma})}{(\epsilon_{k+\gamma} - \epsilon_k)^2(\epsilon_{k-\gamma} - \epsilon_{k+\gamma})} \\ &+ 2\frac{n_F(\epsilon_k)}{(\epsilon_{k-\gamma} - \epsilon_k)(\epsilon_k - \epsilon_{k+\gamma})} \\ &\times \left(\frac{1}{\epsilon_k - \epsilon_{k+\gamma}} + \frac{1}{\epsilon_k - \epsilon_{k-\gamma}}\right) \\ &- 2\frac{n_F'(\epsilon_k)}{(\epsilon_{k-\gamma} - \epsilon_k)(\epsilon_k - \epsilon_{k+\gamma})}.\end{aligned} \tag{B10}$$

In a linear cavity, photons are in a superposition state of two counterpropagating momenta. The interaction with the cavity photons induces two type of processes. The first two lines refer to cycles of absorption and emission where the scattering processes always involve interactions with the same momentum component of the photon field. The other lines refer to scattering processes in which a redistribution of photons between the two momentum components are involved. At the lowest order in γ, the susceptibility χ_3 becomes

$$\begin{aligned}\chi_3(\gamma \ll 1) = \sum_{k\in \mathrm{BZ}} &\frac{\beta^3}{6} n_f(\epsilon_k)[1 - n_f(\epsilon_k)] \\ &\times [1 - 6n_f(\epsilon_k)[1 - n_f(\epsilon_k)]].\end{aligned} \tag{B11}$$

[1] N. Goldman, G. Juzeliūnas, P. Öhberg, and I. B. Spielman, Rep. Prog. Phys. **77**, 126401 (2014).

[2] J. Dalibard, F. Gerbier, G. Juzeliūnas, and P. Öhberg, Rev. Mod. Phys. **83**, 1523 (2011).

[3] P. Engels, I. Coddington, P. C. Haljan, V. Schweikhard, and E. A. Cornell, Phys. Rev. Lett. **90**, 170405 (2003).

[4] V. Schweikhard, I. Coddington, P. Engels, V. P. Mogendorff, and E. A. Cornell, Phys. Rev. Lett. **92**, 040404 (2004).

[5] Y.-J. Lin, R. L. Compton, A. R. Perry, W. D. Phillips, J. V. Porto, and I. B. Spielman, Phys. Rev. Lett. **102**, 130401 (2009).

[6] Y.-A. Chen, S. Nascimbène, M. Aidelsburger, M. Atala, S. Trotzky, and I. Bloch, Phys. Rev. Lett. **107**, 210405 (2011).

[7] P. Hauke, O. Tieleman, A. Celi, C. Ölschläger, J. Simonet, J. Struck, M. Weinberg, P. Windpassinger, K. Sengstock, M. Lewenstein, and A. Eckardt, Phys. Rev. Lett. **109**, 145301 (2012).

[8] N. Goldman and J. Dalibard, Phys. Rev. X **4**, 031027 (2014).

[9] Y. Aharonov and D. Bohm, Phys. Rev. **115**, 485 (1959).

[10] P. G. Harper, Proc. Phys. Soc. Sec. A **68**, 874 (1955).

[11] D. R. Hofstadter, Phys. Rev. B **14**, 2239 (1976).

[12] D. Jaksch and P. Zoller, New J. Phys. **5**, 56 (2003).

[13] M. Aidelsburger, M. Atala, S. Nascimbène, S. Trotzky, Y.-A. Chen, and I. Bloch, Phys. Rev. Lett. **107**, 255301 (2011).

[14] K. Osterloh, M. Baig, L. Santos, P. Zoller, and M. Lewenstein, Phys. Rev. Lett. **95**, 010403 (2005).

[15] M. Aidelsburger, M. Atala, M. Lohse, J. T. Barreiro, B. Paredes, and I. Bloch, Phys. Rev. Lett. **111**, 185301 (2013).

[16] G. Jotzu, M. Messer, R. Desbuquois, M. Lebrat, T. Uehlinger, D. Greif, and T. Esslinger, Nature(London) **515**, 237 (2014).

[17] N. Goldman, J. C. Budich, and P. Zoller, Nat. Phys. **12**, 639 (2016).

[18] D.-W. Zhang, Y.-Q. Zhu, Y. X. Zhao, H. Yan, and S.-L. Zhu, Adv. Phys. **67**, 253 (2018).

[19] N. R. Cooper, J. Dalibard, and I. B. Spielman, Rev. Mod. Phys. **91**, 015005 (2019).

[20] M. Aidelsburger, M. Lohse, C. Schweizer, M. Atala, J. T. Barreiro, S. Nascimbène, N. R. Cooper, I. Bloch, and N. Goldman, Nat. Phys. **11**, 162 (2014).

[21] M. Atala, M. Aidelsburger, M. Lohse, J. T. Barreiro, B. Paredes, and I. Bloch, Nat. Phys. **10**, 588 (2014).

[22] O. Boada, A. Celi, J. I. Latorre, and M. Lewenstein, Phys. Rev. Lett. **108**, 133001 (2012).

[23] A. Celi, P. Massignan, J. Ruseckas, N. Goldman, I. B. Spielman, G. Juzeliūnas, and M. Lewenstein, Phys. Rev. Lett. **112**, 043001 (2014).

[24] H. M. Price, O. Zilberberg, T. Ozawa, I. Carusotto, and N. Goldman, Phys. Rev. Lett. **115**, 195303 (2015).

[25] U.-J. Wiese, Ann. Phys. **525**, 777 (2013).

[26] M. J. Edmonds, M. Valiente, G. Juzeliūnas, L. Santos, and P. Öhberg, Phys. Rev. Lett. **110**, 085301 (2013).

[27] T. Keilmann, S. Lanzmich, I. McCulloch, and M. Roncaglia, Nat. Commun. **2**, 361 (2011).

[28] L. W. Clark, B. M. Anderson, L. Feng, A. Gaj, K. Levin, and C. Chin, Phys. Rev. Lett. **121**, 030402 (2018).

[29] F. Görg, K. Sandholzer, J. Minguzzi, R. Desbuquois, M. Messer, and T. Esslinger, Nat. Phys. **15**, 1161 (2019).

[30] L. Barbiero, C. Schweizer, M. Aidelsburger, E. Demler, N. Goldman, and F. Grusdt, arXiv:1810.02777.

[31] C. Schweizer, F. Grusdt, M. Berngruber, L. Barbiero, E. Demler, N. Goldman, I. Bloch, and M. Aidelsburger, Nat. Phys. **15**, 1168 (2019).

[32] R. Lauter, C. Brendel, S. J. M. Habraken, and F. Marquardt, Phys. Rev. E **92**, 012902 (2015).

[33] S. Walter and F. Marquardt, New J. Phys. **18**, 113029 (2016).

[34] H. Ritsch, P. Domokos, F. Brennecke, and T. Esslinger, Rev. Mod. Phys. **85**, 553 (2013).

[35] K. Roux, H. Konishi, V. Helson, and J.-P. Brantut, Strongly correlated fermions strongly coupled to light, arXiv:1911.11151.

[36] R. M. Kroeze, Y. Guo, V. D. Vaidya, J. Keeling, and B. L. Lev, Phys. Rev. Lett. **121**, 163601 (2018).

[37] Y. Guo, R. M. Kroeze, V. D. Vaidya, J. Keeling, and B. L. Lev, Phys. Rev. Lett. **122**, 193601 (2019).

[38] R. M. Kroeze, Y. Guo, and B. L. Lev, Phys. Rev. Lett. **123**, 160404 (2019).

[39] F. Mivehvar, H. Ritsch, and F. Piazza, Phys. Rev. Lett. **122**, 113603 (2019).

[40] F. Mivehvar and D. L. Feder, Phys. Rev. A **89**, 013803 (2014).

[41] L. Dong, L. Zhou, B. Wu, B. Ramachandhran, and H. Pu, Phys. Rev. A **89**, 011602(R) (2014).

[42] Y. Deng, J. Cheng, H. Jing, and S. Yi, Phys. Rev. Lett. **112**, 143007 (2014).

[43] F. Mivehvar and D. L. Feder, Phys. Rev. A **92**, 023611 (2015).

[44] K. E. Ballantine, B. L. Lev, and J. Keeling, Phys. Rev. Lett. **118**, 045302 (2017).

[45] W. Zheng and N. R. Cooper, Phys. Rev. Lett. **117**, 175302 (2016).

[46] C.-M. Halati, A. Sheikhan, and C. Kollath, Phys. Rev. A **96**, 063621 (2017).

[47] A. Sheikhan, F. Brennecke, and C. Kollath, Phys. Rev. A **94**, 061603(R) (2016).

[48] C.-M. Halati, A. Sheikhan, and C. Kollath, Phys. Rev. A **99**, 033604 (2019).

[49] I. Carusotto and C. Ciuti, Rev. Mod. Phys. **85**, 299 (2013).

[50] J. Keeling, M. J. Bhaseen, and B. D. Simons, Phys. Rev. Lett. **112**, 143002 (2014).

[51] A. Larkin and S. Pikin, Sov. Phys. JETP **29**, 891 (1969).

[52] F. Mivehvar, H. Ritsch, and F. Piazza, Phys. Rev. Lett. **123**, 210604 (2019).

[53] D. Holzmann, M. Sonnleitner, and H. Ritsch, New J. Phys. **20**, 103009 (2018).